Trends in low energy electron microscopy



2010 J. Phys.: Condens. Matter 22 084017

(http://iopscience.iop.org/0953-8984/22/8/084017)

IOP Publishing Journal of Physics: Condensed Matter

J. Phys.: Condens. Matter **22** (2010) 084017 (14pp) doi:10.1088/0953-8984/22/8/084017

# Trends in low energy electron microscopy

**M S Altman**

Department of Physics, Hong Kong University of Science and Technology, Clear Water Bay, Kowloon, Hong Kong

Received 12 April 2009
Published 5 February 2010
Online at stacks.iop.org/JPhysCM/22/084017

**Abstract**

Low energy electron microscopy (LEEM) and spin polarized LEEM (SPLEEM) are two powerful *in situ* techniques for the study of surfaces, thin films and other surface-supported nanostructures. Their real-time imaging and complementary diffraction capabilities allow the study of structure, morphology, magnetism and dynamic processes with high spatial and temporal resolution. Progress in methods, instrumentation and understanding of novel contrast mechanisms that derive from the wave nature and spin degree of freedom of the electron continue to advance applications of LEEM and SPLEEM in these areas and beyond. We review here the basic imaging principles and recent developments that demonstrate the current capabilities of these techniques and suggest potential future directions.

(Some figures in this article are in colour only in the electronic version)

## 1. Introduction

Extensive research of surfaces, thin films and interfaces over the past decades has led to a deeper understanding of many of their fundamental physical and chemical properties as well as an appreciation of the crucial role that they can play in numerous applications. Among the assorted experimental tools that are available, several microscopies have played an important part in the identification and explanation of many complex phenomena at surfaces and in thin films. In addition to the widely known scanning probe microscopy (SPM) and scanning electron microscopy (SEM) techniques, low energy electron microscopy (LEEM) is another important, though less common, imaging technique that has contributed significantly to advances in this discipline. Since its invention by Bauer [1], LEEM has developed into one of the premier techniques for *in situ* studies of surface structure, morphology and dynamical processes [2–6]. LEEM is foremost a type of cathode lens electron microscopy. This designation refers to the group of microscopies in which the sample serves actively as a cathode element that emits electrons in the objective lens of the microscope. In contrast to the more common scanning surface microscopies mentioned above, LEEM and related cathode lens microscopies are non-scanning techniques. Information is obtained simultaneously at every point in the image. Electron emission from the sample in cathode lens microscopy is stimulated by any of several means, for example, by excitation using photons, electrons, ions or other incident particles and via elastic or inelastic scattering processes as well as by thermal emission. In LEEM, elastic backscattering of a coherent, monoenergetic low energy electron beam produces a high reflected electron intensity. Coupled with the non-scanning image formation mechanism, the high reflected intensity of low energy electrons facilitates imaging in real-time on a timescale that defines the scope of LEEM applications. For the case of crystalline samples, elastic electron scattering is accompanied by diffraction, such that complementary low energy electron diffraction (LEED) measurements can be performed in a LEEM instrument. The use of low energy electrons has the additional implication that the penetration depth is shallow and the measurement is surface-sensitive. In order to take full advantage of this surface sensitivity, LEEM is fully ultra-high vacuum-compatible. Other forms of cathode lens microscopy that are worth mentioning briefly here are mirror electron microscopy (MEM) and photoemission electron microscopy (PEEM). In MEM, the incident electron beam is completely reflected at an equipotential surface within the objective lens in front of the sample surface and the 'mirror' reflected beam is used to form an image. In PEEM, photons are used to excite photoelectrons for imaging purposes. Several powerful variants of the PEEM technique have been developed using laboratory and particularly synchrotron-based light sources. Each different microscopy variant has its own advantage and realm of application. The range of applications of a microscopy is determined largely by its spatial resolution and contrast mechanisms, while image acquisition time can also be of importance in some problems. Although PEEM, MEM and other cathode lens microscopies can be performed in an LEEM instrument, this paper focuses on LEEM and a closely

 

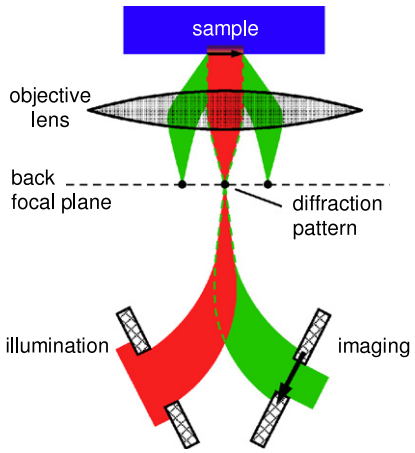


**Figure 1.** Schematic diagram of electron beam trajectory, image and diffraction pattern formation in the LEEM objective lens and sector field regions. The hatched rectangles are apertures.

related technique that harnesses the spin degree of freedom of the incident electron beam, called spin polarized LEEM (SPLEEM).

## 2. LEEM imaging principle

As a basis for discussing past work with a view towards potential future applications of the LEEM technique, we begin with a brief description of its imaging principle, contrast mechanisms, resolution and other relevant issues. Aspects of various instrumentation solutions are described in numerous papers [2, 7–16].

LEEM images surfaces with elastically backscattered low energy electrons. In the context of crystalline samples, elastic backscattering of a coherent electron beam produces diffraction. Thus, LEEM can provide access to complementary real space and reciprocal space information. This information is obtained alternatively by imaging the surface or LEED pattern through an appropriate setting of the electron-optical elements in the microscope. The image and diffraction pattern are formed as follows. An electron beam is first generated by a cathode in the electron gun and accelerated to the microscope potential, typically 15–20 keV. The electron-optical elements in the illumination column are used to form a collimated electron beam suitable for illumination of the sample. Before reaching the sample, however, the beam is deflected by a magnetic sector field to a trajectory on the optical axis of the objective lens and normal incidence to the sample. In the backscattering LEEM geometry, the incident and reflected beams pass through the objective lens in opposite directions (figure 1). The sector field solves the problem of separating the reflected beam from the incident beam outside of the objective region.

The incident electron beam is focused by the illumination optics to a crossover point in the back focal plane of the objective lens (figure 1). The objective lens acts on the incident and reflected electron beams together and serves a dual purpose in both cases. It focuses the incident beam to a parallel beam or plane wave at the sample and decelerates the beam to the desired incident energy. The incident energy is determined by the variable bias between the sample and the electron gun cathode potentials. The reflected electrons are then reaccelerated to the microscope potential and also focused by the objective. For crystalline samples, electron reflection is confined to specific angles by diffraction, i.e. the Bragg angles. Electrons that are emitted at the same angle are focused to points in the back focal plane. This amounts to the formation of a diffraction pattern in the back focal plane. Various objective lens configurations have been used that differ in their spatial resolution and transmission [16]. After emerging from the objective lens, reflected electrons are deflected by the sector field into the imaging column. An image is present in the middle of the sector field (figure 1) and the diffraction pattern is reproduced at a secondary diffraction plane within the imaging column by a transfer lens at the front of the column. An image is formed by selecting one of the diffracted beams using a contrast aperture in the diffraction plane. The imaging column optics are suitably adjusted to magnify the image residing in the sector field onto the microchannel plate/phosphor screen detector. Alternatively, the diffraction pattern can be observed by removing the contrast aperture and adjusting the optics to obtain an image of the diffraction plane.

The normal incidence/exit geometry that is shown explicitly in figure 1 is depicted in the reciprocal space diagram in figure 2(a). The diffraction condition is specified by the momentum transfer, $\Delta k = k_f - k_i$, where $k_i$ is the wavevector of the incident beam and $k_f$ is the final wavevector after scattering. In surface diffraction, diffraction intensity may be found possibly for any perpendicular momentum transfer, $\Delta k_\perp$, along diffraction rods that are oriented perpendicular to

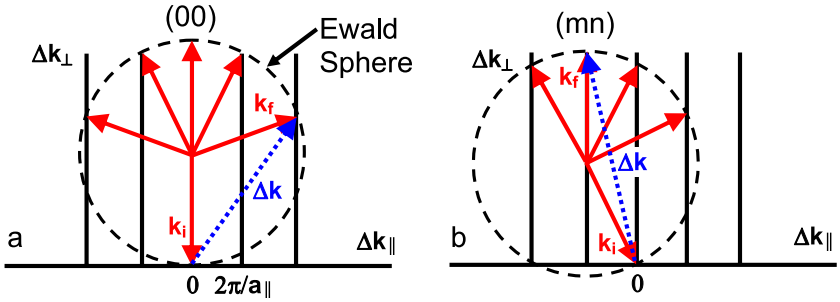


**Figure 2.** Reciprocal space representation of surface diffraction for (a) normal incidence (bright-field) and (b) off-normal incidence (dark-field).

the surface and positioned at values of the parallel momentum transfer, $\Delta k_{\parallel}$, that are determined by the surface periodicity. The normal incidence/exit condition that is used most often for LEEM imaging, but not always, corresponds specifically to diffraction along the rod labeled (00) in figure 2(a). This is the so-called bright-field imaging mode corresponding to no momentum transfer parallel to the surface. Alternatively, diffraction conditions along fractional order superstructure or low order integer order diffraction rods may be used to form images in the dark-field imaging mode. In practice, this is achieved by tilting the illumination, $k_{\rm i}$, off-axis by an angle that puts the imaging beam, $k_{\rm f}$, along a trajectory normal to the surface (figure 2(b)). By keeping the imaging beam on the optical axis of the objective lens in this way, image distortion due to spherical aberration of the objective is avoided. The bright-field and dark-field imaging modes are discussed below in the context of image contrast.

Although imaging using low energy electrons necessitates the reflection geometry and the added complexity of the sector field in the first place, it brings key advantages. As noted before, surface sensitivity is a result of the short penetration depth of electrons at low energy. The universal curve for the electron mean free path indicates a minimum probing depth of only 1–2 atomic layers at 50 eV [17]. However, the mean free path also rises sharply to several nm at a few electron volts. Thus, it is possible, in principle, to probe deeper layers and buried interfaces by working at such low energies. Another benefit of using electrons in the very low energy range is that their reflectivity can be very high. Several factors contribute to the high reflectivity, including details of the atomic scattering factor for electrons [17], angular confinement by diffraction, the Debye–Waller factor and extinction of higher-order diffraction conditions. Combined with the non-scanning imaging mechanism, this equates to short image acquisition time and real-time imaging capability.

## 3. Resolution and contrast

While image acquisition time can be of importance in some imaging applications, resolution and contrast are generally the two most important aspects in imaging that define the applications of a microscopy technique. In the past, most of the attention has been given to calculating resolution using ray-optical methods. Calculations for the ideal homogeneous accelerating field exposed the impacts of diffraction at the contrast aperture, chromatic and spherical aberrations on LEEM resolution [18]. The general findings are that LEEM is diffraction-limited at very low energy because of the inverse square root relationship between wavelength and energy, $\lambda \sim E^{-1/2}$. Chromatic aberrations, which arise from the energy dependence of the objective lens' focal length, also degrade resolution for typical energy spreads of conventional electron sources. Spherical aberrations, which arise from focusing errors of the objective lens for waves that travel at angles from the optical axis, are unimportant in LEEM in comparison to diffraction error and chromatic aberration because electrons are largely confined to the optical axis by diffraction at the crystal surface. Although spherical aberrations generally become more important at higher energy, LEEM resolution generally improves at higher imaging energy due to the diminishing effects of the other factors. However, the useful imaging energy range is limited at higher energy by intensity considerations.

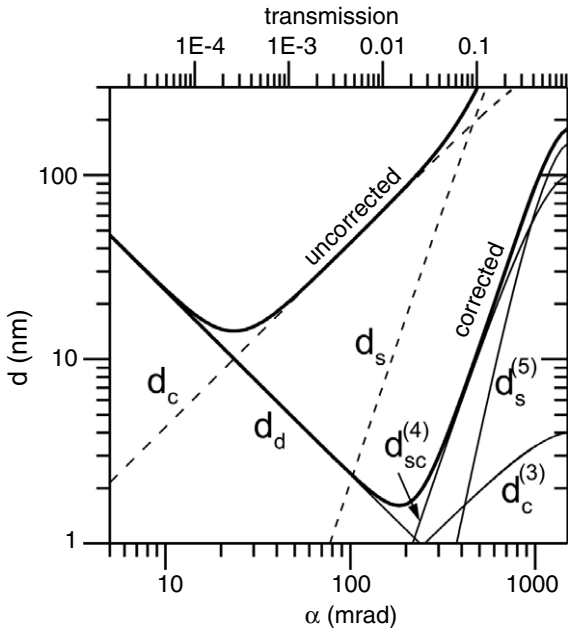


**Figure 3.** Resolution, $d$, of uncorrected and aberration-corrected instruments (thick solid lines) as a function of the acceptance angle, $\alpha$, for imaging energy $E_0 = 10$ eV and energy spread $\Delta E = 2$ eV. The contributions to resolution of the lowest-order aberrations, $d_{\rm c}$ and $d_{\rm s}$ (dashed lines), diffraction limit, $d_{\rm d}$, and higher-order aberrations, $d_{\rm sc}^{(4)}$, $d_{\rm c}^{(3)}$ and $d_{\rm s}^{(5)}$ (thin solid lines), are shown. The lowest-order aberrations that dominate for the uncorrected instrument are eliminated in the corrected instrument. Reproduced with permission from [21]. Copyright 2002 by World Scientific.

A comparison of the resolution for various objective lens designs has been made [16]. Except for the electrostatic tetrode which is currently used in SPLEEM, magnetic objective lenses have overtaken electrostatic lenses in conventional LEEM instruments because of their superior spatial resolution. This is a result of the higher field strength that can be applied between the objective and the sample, which accelerates the emitted electron beam. Although less important for LEEM than for PEEM, magnetic objective lenses also provide higher transmission. Another important step that has been taken to improve resolution is to reduce the energy spread, $\Delta E$, of the incident electron beam. Compared to current instruments that deliver a resolution of 5–7 nm in the useful range of imaging energy using $LaB_6$ cathodes ($\Delta E \sim 0.7$ eV), the influence of chromatic aberrations is diminished somewhat but not eliminated altogether through the use of a field emission source ($\Delta E \sim 0.5$ eV). Instrumental resolution that is achieved in practice using a field emission source is between 4 and 5 nm.

Spurred by the potential for opening new avenues of research using LEEM at shorter length scales, an even more radical approach has been taken in recent years to improve resolution. That is done by incorporating electrostatic mirror elements [19] that correct lowest-order chromatic and spherical

aberrations of the objective lens [20–22]. The influences of the various factors that define the resolution of corrected and uncorrected instruments are shown in figure 3. Although this figure is calculated for an energy spread of 2 eV, which is too large by a factor of 4 for LEEM, it still serves an important illustrative purpose. In this figure, the diffraction limit, $d_d$, and lowest-order chromatic and spherical aberrations, $d_c$ and $d_s$, respectively, define the resolution of an uncorrected instrument. After correction of these lowest-order aberrations, the remaining higher-order aberrations, $d_{sc}^{(4)}$, $d_c^{(3)}$ and $d_s^{(5)}$ defined in [21], become important. This figure demonstrates that a resolution below 2 nm can be achieved in a corrected instrument. For smaller energy spread, the $d_c$, $d_c^{(3)}$ and $d_{sc}^{(4)}$ curves will be shifted downward proportionately and the calculated resolutions will be correspondingly better. This figure also illustrates how the optimum acceptance angle, $\alpha$, which is proportional to the diameter of the contrast aperture, is defined by the balance of the diffraction limit and aberrations. This is the reason for the higher transmission in corrected instruments. Until now, the world record resolution achieved using an aberration-corrected instrument, specifically the one represented in figure 3, is 2.6 nm, which is sufficient to resolve the herringbone structure periodicity on the reconstructed Au(111) surface [23].

Further improvements may be achieved by the reduction of mechanical and electrical instabilities. Typical current and voltage instability levels are on the order of $\Delta I/I = \Delta U/U = 10^{-5}$. A Fourier optics calculation of image formation in LEEM using a magnetic objective lens has shown that instabilities at this level have a negligible effect on the resolution of the uncorrected instrument [24]. Figure 4 demonstrates the improvement of resolution that can be achieved by first-order aberration correction and reduction of current/voltage instabilities within the context of the Fourier optics calculation. This figure presents the calculated intensity profiles of a pure amplitude object for the uncorrected instrument with an instability level of $10^{-5}$, and for the corrected instrument with instabilities of $10^{-5}$ and $10^{-6}$. It shows how the resolution, given by the sharpness of the intensity step profile, is improved significantly by aberration correction and further improved by the reduction of instabilities. It should be noted, however, that the calculation considers the chromatic and spherical aberrations of lowest order only. Higher-order aberrations that determine resolution in aberration-corrected instruments are not taken into account. Nevertheless, the result is still strongly suggestive that reduction of voltage and current instabilities by an order of magnitude, which is not an unreasonable proposition, may bring some practical benefit for achieving the optimal resolution of aberration-corrected instruments.

Several contrast mechanisms can be exploited for imaging that derive from the amplitude and phase of the electron wave in LEEM as well as the spin degree of freedom of the electron in SPLEEM. Sample features that produce a spatial variation of the amplitude of the reflected wave generate what has been alternatively called amplitude, reflectivity or diffraction contrast. This is arguably the most frequently used contrast mechanism in LEEM. It arises when there

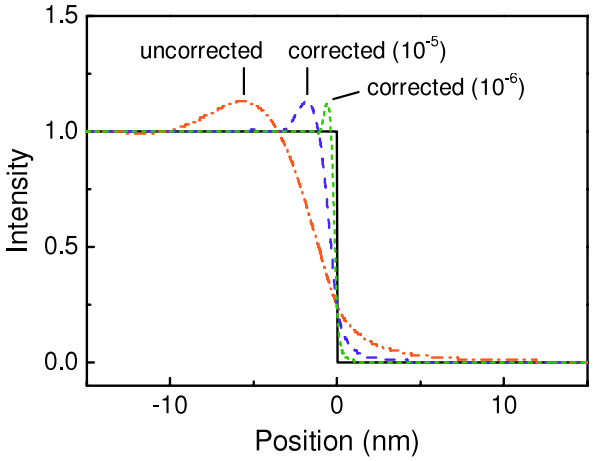


**Figure 4.** Image intensity profile of a pure amplitude object (solid line) calculated by Fourier optics for an uncorrected instrument with voltage and current instabilities $\Delta I/I = \Delta U/U = 10^{-5}$ (dotted–dashed curve), aberration-corrected instrument with instabilities of $10^{-5}$ (long dashed curve) and $10^{-6}$ (short dashed curve).

are different structures or materials present with different reflection coefficients. This may occur, for example, because the diffraction intensities are different under the same diffraction condition. Diffraction contrast may be observed in either the bright-field or dark-field imaging modes that were mentioned previously (figure 2). Very often, sufficient contrast can be found at some imaging energy in bright-field mode to distinguish different structures. When this is not the case, dark-field imaging can provide an attractive alternative. For example, dark-field can be used to distinguish domains of a single structure that are related by a rotation about an axis normal to the surface. In the case of rotational domains, the diffracted intensity along the (00) rod used for bright-field imaging is identical at all energies due to symmetry. In dark-field imaging, the use of diffraction conditions along a fractional-order superstructure rod or integer-order rod with non-zero parallel momentum transfer breaks the symmetry between rotational domains. Any region on the surface that scatters strongly in the diffraction condition used for dark-field imaging will appear bright in the image, while regions that scatter weakly or for which the diffraction condition is forbidden will appear dark. The dark-field imaging mode was first demonstrated in experiments that distinguished (5 × 1) reconstructed domains on an Au(100) surface and in Au films on Si(111) [25, 26]. It has also been instrumental in numerous investigations of the Si(100) (1 × 2) reconstructed surface [4, 27–34]. For this system, the surface structure alternates between (1 × 2) and (2 × 1) periodicity on adjacent terraces separated by an atomic step, due to the diamond crystal structure of bulk Si. Thus, dark-field imaging distinguishes adjacent terraces and identifies the locations of intervening atomic steps. Dark-field imaging using integer-order diffraction conditions has also been demonstrated. Under these conditions, contrast between adjacent terraces separated by a bilayer height step was observed at the GaN(0001) surface [35]. This contrast arises because the bulk stacking

in wurtzite materials produces a 60° rotation of the hexagonal unit cell across a bilayer high step. Twinned epitaxial Si islands grown on the Si(111)-B $(\sqrt{3} \times \sqrt{3})$R30° surface that are rotated by 180° with respect to the substrate were also detected using integer-order dark-field imaging conditions [36]. Similar integer-order dark-field imaging of the Ru(0001) surface exhibited contrast between terraces separated by a single atomic step [37]. These examples demonstrate the potential of integer-order dark-field imaging for studying near-surface bulk stacking, a capability that will clearly be of use for research on complex materials such as compound semiconductors in the near future.

Modifications of the phase of the imaging electron wave that occur upon reflection from the sample can also be harnessed to obtain image contrast. This produces phase contrast in LEEM when it leads to interference effects. A surface step is an example of a pure phase object that causes a phase shift but has no effect on the wave amplitude. The phase shift is given by $\phi = kd = (2\pi/\lambda)2a_0$, where $d = 2a_0$ is the path length difference between waves that are reflected from terraces on the opposite sides of a step, $a_0$ is the step height and $\lambda$ is the wavelength of low energy electrons that are elastically backscattered from the surface. Step phase contrast has been observed on many surfaces and has been instrumental in numerous studies of surface morphological evolution (see section 4).

The underlying interference phenomenon has been explored further using a wave-optical model [38, 39]. A surface step is modeled in this approach as two opposed, semi-infinite apertures that are oriented perpendicular to an illuminating wave and shifted by the step height in the direction parallel to the illumination. Step contrast is calculated as the interference of the Fresnel diffracted waves that are produced at the two aperture edges. This model reveals that a rich interference phenomenon is caused by a step. Step contrast is generally characterized by an oscillatory variation of intensity with features near to the step that depend fundamentally upon phase shift (figure 5), i.e. wavelength and electron energy, and focus condition. The intensity profiles shown in figure 5 were calculated for a step configured with the terrace on the lower or step-down-side at positive coordinates. The model calculation was carried out in a way that corresponds to LEEM imaging in the underfocused condition (focal length is increased by reducing the lens excitation compared to the in-focus condition). The rich interference patterns shown in figure 5 were obtained from model calculations that assumed a perfectly coherent source and aberration-free imaging. When finite beam coherence and lens aberrations were included in an approximate way, only the strongest interference fringes immediately adjacent to the step were obtained. This result closely resembles experimental observations. In the out-of-phase conditions, $\phi = (2n + 1)\pi$, where $n$ = integer, complete destructive interference occurs at the step position and equivalent intensity maxima are located symmetrically on both sides of the step. In the in-phase condition, $\phi = 2n\pi$ contrast is absent. Clearly asymmetric features are observed at the intermediate phase conditions that are most pronounced at $\phi = (2n + 1)\pi/2$. For

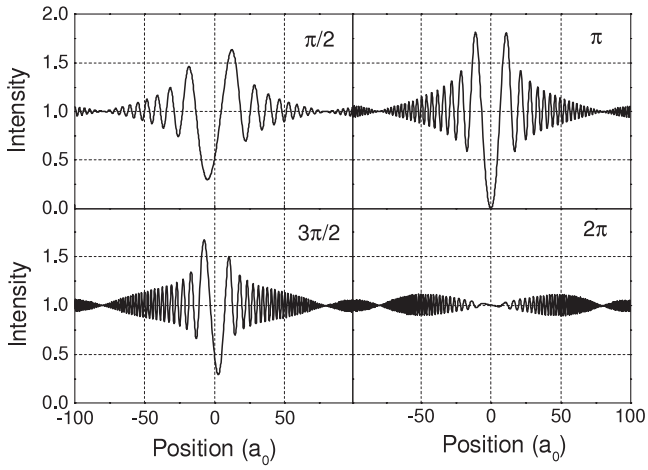


**Figure 5.** Step phase contrast calculated using a wave-optical model for several values of phase shift at a step at underfocus imaging conditions. The step is located at the 0-position and the terrace at the down-side of the step is located at positive coordinates. Position is expressed in units of the step height, $a_0$ (adapted from [38]).

$\phi = \pi/2$ and equivalent conditions ($n$ = even), an intensity maximum (minimum) is located on the down- (up-)side of the step for underdefocus. For $\phi = 3\pi/2$ and equivalent conditions ($n$ = odd), the asymmetry is reversed with an intensity maximum (minimum) located on the up- (down-)side of the step for underdefocus. The asymmetries at the two intermediate phase conditions for overfocus condition are also reversed from those depicted for underfocus in figure 5. This understanding of asymmetric step phase contrast features allows for the identification of the step sense, i.e. which is the up-side and which is the down-side, simply by visual inspection of the image.

Another important phase contrast mechanism occurs in LEEM for thin films due to the quantum size effect (QSE) in electron reflectivity [40–43]. The QSE in electron reflectivity can be understood to be caused by the interference between the electron waves that are reflected from the surface of a film and from the interface between film and substrate. This interference arises because the path length for the two participating waves differs by $d = 2t$, where $t$ is the film thickness. The path length difference produces a phase shift between the waves, $\phi = k'd$, where the wavevector in the film, $k'$, is given by the band structure. Consequently, the reflected intensity is modulated both as a function of the incident electron energy and as a function of the film thickness.

In LEEM, the QSE in electron reflectivity gives rise to a vivid quantum size contrast between regions of different film thickness (figure 6) [39, 44–64]. Due to the energy dependence of the QSE, quantum size contrast also varies strongly with small changes of the incident electron energy. By varying the incident electron energy and measuring the reflected intensity in uniformly thick regions within the image field of view, single-layer thickness $I(V)$ curves of the (00) beam are obtained. Prominent quantum interference peaks (QIPs) can be observed in the reflected intensity at incident electron energies that correspond to in-phase interference conditions, $\phi = 2n\pi$, where $n$ = integer (figure 6). The number and energies

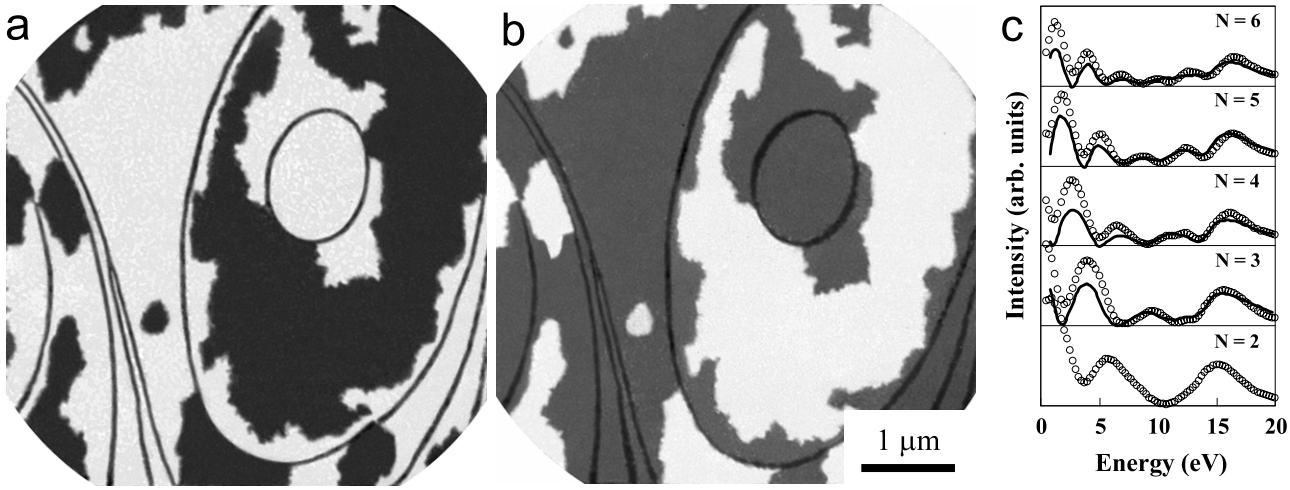


**Figure 6.** LEEM images that show quantum size contrast between 2 and 3 ML Ag regions on the W(110) surface at imaging energies of (a) 5.8 eV and (b) 9.8 eV. The dark lines are monatomic steps generated at the Ag/W interface. In (c), the reflected image intensity exhibits quantum interference peaks due to the quantum size effect in electron reflectivity for $N = 2$–6 layer Ag films on W(110) determined in experiment (○) and by dynamical theory analysis (solid curves). A Bragg peak is present at 16 eV. Reproduced with permission from [48]. Copyright 2003 by the American Physical Society.

of QIPs depend dramatically on the number of atomic layers in the film. As a simple rule-of-thumb, there are $N - 1$ QIPs between successive Bragg peaks for an $N$-layer film. Thus, film thickness in terms of the number of atomic layers can be assessed simply by counting the number of QIPs. In principle, QIPs may exist between any two successive Bragg peaks at all energies. However, in practice QIPs become very weak at higher energy where the electron mean free path in the film is short and the reflectivity from the buried interface becomes weak in comparison to the reflectivity of the film surface. That is why it is crucial to work in the very low energy range, below about 30 eV, where the mean free path increases sharply with decreasing energy in order to observe QIPs. The occurrence of quantum size contrast at very low energy is also conditional on high reflectivity from the buried interface. This can arise if a bandgap or $\Delta_1$ symmetry gap is present in the substrate band structure in the relevant energy range for $\Delta k_{\|} = 0$ or if there is a large potential step between film and substrate. Such conditions have been observed to produce quantum size contrast in many systems including Cu/Mo(110) [44], Co/W(110) [45, 54], Cu/W(110) [39, 46, 56], Ag/W(110) [46, 48, 52, 59], Fe/W(110) [47, 54], Mg/W(110) [50, 60], Sb/Mo(100) [46], Ag/Fe(100) [49], MgO/Fe(100) [57], Cu/Co/Cu(100) [53], Cu/Ru(0001) [51], Ag/Ru(0001) [51, 55, 58], Au/Ru(0001) [58], AgAu/Ru(0001) [58], graphene on SiC(0001) [61, 62, 64] and exfoliated graphene [63].

The discrimination of information from regions of different film thickness via LEEM quantum size contrast facilitates the comparison of experimental data to model calculations for idealized uniformly thick films. This has been exploited, for example, to determine the details of layer spacings down to the buried interface layer by full dynamical multiple scattering analysis of QIPs [48]. QIPs are also associated with quantum well (QW) resonances above the vacuum level. The dependence of QW resonances on film thickness and energy can be understood by the phase accumulation model [47, 49, 52, 53], which was developed earlier to describe the binding energies of QW states below the Fermi level [65]. Analysis of QW resonance conditions that are identified by the QIPs using the phase accumulation model has provided information on unoccupied band structure above the vacuum level in several systems [47, 49, 52, 53, 56, 57, 61]. Quantum size contrast has also been used to study the influence of QW states on film morphology [49], growth and morphology of graphene on SiC(0001) [61, 62, 64].

The conventional LEEM diffraction and phase contrast mechanisms are augmented by magnetic contrast when a spin polarized electron beam is used to illuminate the surface [2, 5, 6, 11, 12, 66–70]. The magnetic sensitivity of spin polarized LEEM (SPLEEM) stems from spin-dependent exchange scattering. The exchange asymmetry is defined as $A_{ex} = (1/P)(I_\uparrow - I_\downarrow)/(I_\uparrow + I_\downarrow)$, where $I_\uparrow$ and $I_\downarrow$ represent the reflected intensities for oppositely polarized incident beams, called spin-up and spin-down, and $P$ is the degree of spin polarization of the incident beam. Subtraction of spin-up and spin-down images in the numerator eliminates non-magnetic diffraction and topographical image features that are found in conventional LEEM images and leaves features that originate exclusively in the magnetism of the sample. Division by the spin-up and spin-down image sum yields an asymmetry image in which intensities are proportional to $1/P$ and the component of the local magnetization vector that lies along the incident beam polarization direction.

A longitudinally polarized electron beam is generated by illumination of a GaAs photocathode [71] with circularly polarized light having wavelength matched to the cathode bandgap. Although the maximum polarization that can be achieved in principle using bulk GaAs is 50%, polarization closer to 25% is typically obtained. Higher spin polarization can be achieved by various approaches that lift conduction band degeneracies through symmetry breaking, including the

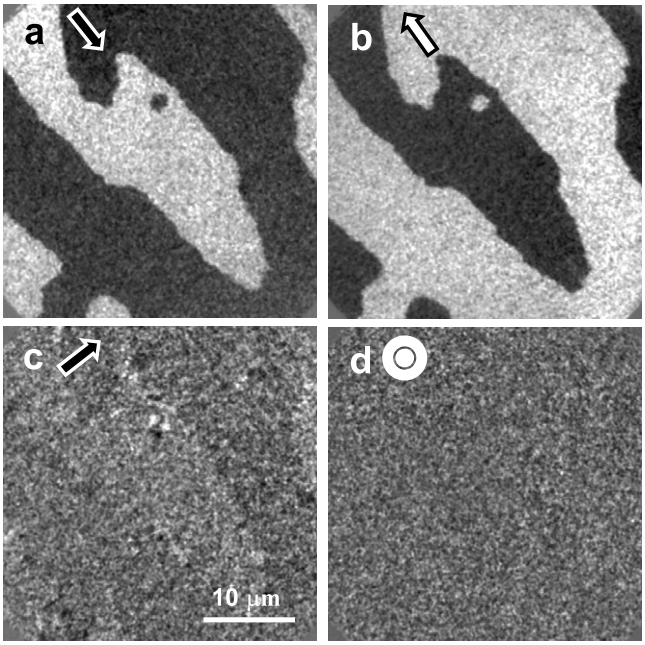


**Figure 7.** SPLEEM images of uniaxial in-plane magnetic domains in a Co film on a vicinal W(111) surface are shown for indicated (a)–(c) in-plane and (d) out-of-plane incident beam polarization directions. Reproduced with permission from [79]. Copyright 2003 by the American Physical Society.

use of strained layer cathodes [72, 73] and multilayers [74–77]. The spin polarization direction can be reversed by 180° by changing the sense of circular polarization of the illumination between left-and right-handed. In addition, a SPLEEM instrument incorporates a spin manipulator [78] consisting of combined electrostatic and magnetic deflectors and a magnetic rotator lens. The spin manipulator elements can be used to adjust the azimuthal and polar angles of the incident beam spin direction fully relative to its propagation direction. This allows complete characterization of the sample magnetization direction in the in- and out-of-plane directions and tilted directions in between. As an example of this capability, step-induced uniaxial domains in a Co film on the W(111) surface are shown in figure 7 [79].

SPLEEM has been used to address a variety of problems including numerous aspects of magnetic domain and domain wall structure in thin magnetic films and surface-supported nanostructures [79–91], exchange coupling [92, 93], spin reorientation transition [81, 86, 94–98], phase transitions and finite size effects [84, 85, 99]. SPLEEM has also been used to study spin-dependent electron reflectivity and spin-resolved quantum well resonances in magnetic films [45, 47, 53, 54, 57]. One possible deficiency of SPLEEM is that the low energy electrons used for imaging are sensitive to the presence of non-axial magnetic fields. This has limited its application to the study of magnetic structures in their spontaneously or remanently magnetized states. Nevertheless, it has been shown that it is possible to image using SPLEEM with moderate applied fields normal to the surface [100]. Imaging under these conditions is possible because the Lorentz force that acts on imaging electrons is zero where the field lies parallel to the incident and reflected electron trajectory. Modest field of several tens to one hundred gauss may be achieved in these imaging conditions. The imaging capability of SPLEEM is also compromised somewhat compared to conventional LEEM because of the photocathode source characteristics. The effective large source size, which is defined by the laser illumination, results in low brightness compared to conventional field emission and LaB6 cathodes. In order to address this deficiency, work has been carried out recently to develop a back-illuminated spin polarized electron source [75–77]. In this geometry, the laser spot size can be reduced significantly by placing a focusing lens considerably closer to the cathode than in the conventional front-illuminated geometry. A spin polarized electron gun based on this concept that is currently being tested in a SPLEEM instrument is producing promising results [101]. This development is expected to improve image quality modestly and to improve imaging rate markedly.

## 4. Surface dynamics

Fast image acquisition with LEEM facilitates remarkable real-time observations of dynamic processes at surfaces. The timescale of the measurement, which has a lower bound that is determined by the imaging rate (up to video rate ∼25–30 frames $s^{-1}$), defines the types of phenomena that are accessible to LEEM. This opens the possibility to address a large number of problems involving collective atomic processes. Numerous examples of previous applications illustrate the possibilities. In broad strokes, this includes, but is not limited to, the study of phase transitions [102–110], self-organization and pattern formation [31, 32, 111–120], diffusion, mass transport and morphological evolution during growth, coarsening and sublimation [30, 33, 34, 49, 51, 121–144], fluctuation spectroscopy [29, 32, 114, 145, 146], surface alloying [110, 111, 113, 147–150], chemical reactions and oxidation [135, 152–157].

A hallmark of many of these studies is the quantitative evaluation of relevant physical parameters, which is accomplished by the analysis of the real-time observations. Approaches that have been taken in this respect have examined both equilibrium and non-equilibrium behavior. A prominent example of the former is the extraction of step line tension from equilibrium fluctuations of surface steps using capillary wave theory [29, 32, 145, 146]. Similar analysis has also been applied to evaluate equilibrium domain wall fluctuations [114]. These types of investigations are of note because they push the measurement capability of LEEM to its spatial and temporal resolution limits. The analysis of equilibrium fluctuations typically begins by defining different fluctuation modes, $q$, through a Fourier transform of the object configuration at time $t$. Step or domain wall energetics are obtained from a time series of Fourier amplitudes for the different modes by either of two methods. First, it is proportional to the inverse of the time-averaged squared Fourier amplitude. Each Fourier mode should lead to the same result based on the equipartition theorem, provided that the mode is not adversely affected by

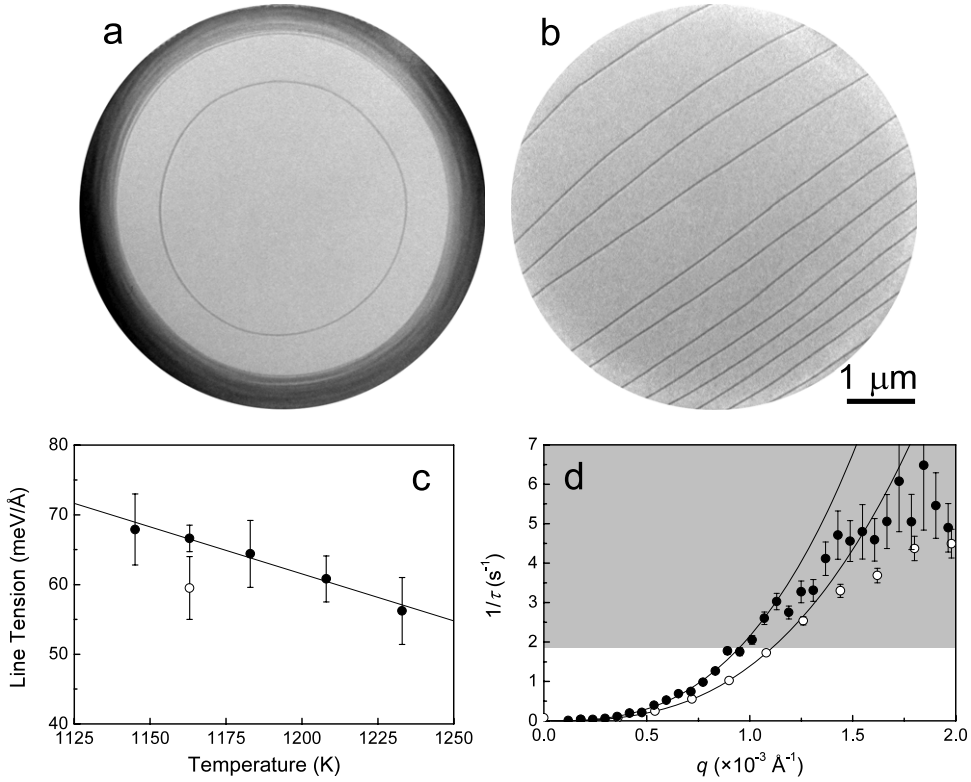


**Figure 8.** LEEM images of (a) a monatomic height island and (b) straight monatomic height steps on the Si(111) (1 × 1) surface at 1163 K. (c) The step line tension determined from island (●) and straight step (○) fluctuations is shown as a function of temperature. (d) The dependence of the inverse relaxation time upon mode is shown for island (●) and straight step (○) fluctuations at 1163 K. The gray shaded area indicates the temporal regime that is shorter than the image integration time. The best fits of the dynamic scaling power law are indicated by solid lines. Reproduced with permission from [146]. Copyright 2008 by the American Physical Society.

the time resolution of the measurement. Alternatively, it can be determined from the mode-dependent amplitude of the time correlation function $A(q) = 2kT/L(\tilde{\beta}q^2 + c)$, where $k$ is the Boltzmann constant, $T$ is temperature, $L$ is the length of step or boundary object being analyzed and $c$ is a constant that is related to interactions between neighboring objects. In the case of step fluctuations, mode-dependent relaxation times that are obtained from an evaluation of the temporal correction function also provide information about the rate-limiting kinetics that mediate step motion. The relaxation time is described by the dynamical scaling relationship $\tau(q) = \tau_0(z)q^{-z}$, where different integer values of the dynamical exponent $z$ and correspondingly different forms of $\tau_0$ are valid for different dominant kinetic mechanisms.

In the past, fluctuation spectroscopy has been carried out mostly for nominally straight objects. Recently, this analysis has been extended using LEEM to the case of steps at the edges of two-dimensional islands [146]. One advantage of focusing on island edge fluctuations is that the perimeter of an island can be longer than a straight step that spans the same field of view. This imparts higher resolution of the fluctuation modes, $q = 2m\pi/L$, where $m =$ integer. Consequently, more modes are available for analysis in the spectral window that is imposed by the temporal resolution limit. Other advantages and disadvantages of the island geometry and their mitigation have been discussed [146]. A comparison of results for step line tension and the $q$ dependence of the relaxation time for straight steps and for island edges is shown together with the respective step configurations in figure 8. This demonstrates the validity of island edge fluctuation analysis and the higher $q$ resolution afforded by the island geometry, which helps to make the most of the temporal resolution of the technique.

In non-equilibrium methods, the surface is established in some non-equilibrium configuration or condition and the change of some feature in response to this non-equilibrium state is observed. A convenient and frequently observed surface feature under such non-equilibrium conditions is atomic surface steps. Non-equilibrium conditions that have been investigated include island nucleation and step motion during growth under a deposited flux, sublimation, island coarsening driven by the Gibbs–Thomson effect and under mass exchange between surface and bulk (figure 9). A recent development in this area is the coupling of accelerator to LEEM for the purpose of *in situ* irradiation with self-ions with variable energy [143]. This allows for the net deposition of atoms or vacancies by controlling the energy of the incident ion beam. Thus, it is possible to investigate atom or vacancy diffusion and mass transport behavior, among other things.

Paramount to the quantitative interpretation of phenomena involving mass transport, such as step motion, is knowledge of the spatial concentration or chemical potential variation of the species that mediates mass transport. In the past, this has been obtained, for example, by solution of the diffusion equation subject to assumptions about relevant kinetic processes. Thus,

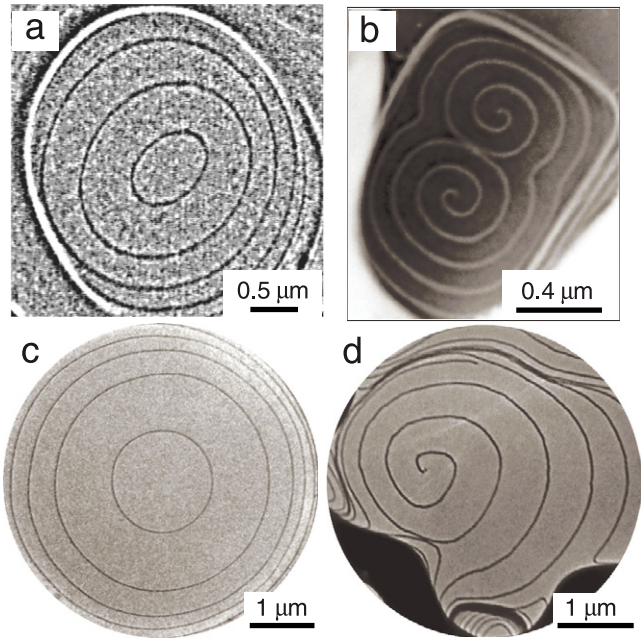


**Figure 9.** Island coarsening (a) on the Ni Al(110) surface at 957 K (reproduced with permission from [125]. Copyright 2001 by the Nature Publishing Group.) and (c) the Si(111) (1 × 1) surface at 1163 K (reproduced with permission from [138]. Copyright 2007 by Elsevier.) Screw spiral motion (b) on the Cr(100) surface during sublimation at 1166 K (reproduced with permission from [133]. Copyright 2006 by the American Physical Society.) and (d) on TiN(111) at 1710 K (reproduced with permission from [130]. Copyright 2004 by the Nature Publishing Group.).

the forgoing methods are indirect and prone to error if incorrect assumptions are made. Although tremendous impact has been made in this avenue of research by such methods, this situation begs for the development of techniques that visualize concentrations directly. One recent development in this direction exploits the fact that the presence of an adatom gas causes diffuse scattering of electrons and a complementary loss of intensity in the image-forming diffraction beam in proportion to concentration [2, 134, 139]. Measurements have shown that coverage changes as small as $10^{-3}$ monolayer (ML) can be detected by this method. It can therefore be harnessed in principle to obtain spatial concentration contrast, although this has not been achieved yet.

Another approach to this problem that also exploits the coverage dependence of the reflected intensity employs LEEM to monitor the temporal evolution of non-equilibrium coverage profiles that are prepared by laser-induced thermal desorption (LITD). Non-equilibrium profile evolution methods have been used for many years to study diffusion and mass transport. Various methods have been used in the past to prepare non-equilibrium profiles and to monitor their evolution. One advantage of using LEEM to monitor profile evolution is that it allows for characterization of profile shape with high spatial resolution. It can also provide complementary information on surface structure and morphology that is typically accessible to LEEM. This additional information, which is not available to laterally averaging methods, may prove to be valuable for interpreting profile evolution behavior. The LEEM-based method has been used to study diffusion and mass transport in CO/Pt(111) [140] and Pb/Si(111) [141]. In these cases, it appears that the coverage contrast comes from the effect of adsorbate on the structure factor for elastic scattering, as shown by changes in the $I(V)$ curve intensity peak heights and positions, rather than from diffuse scattering. The relationship between image intensity and coverage is calibrated by measuring intensity during exposure or deposition on the surface. Special care must be taken in the case of gas adsorbates to take account of the coverage-dependent sticking coefficient in order to relate intensity to coverage. Sensitivity of this contrast mechanism to coverage changes of the order of $10^{-4}$ ML was demonstrated [140]. LITD uses a single laser pulse to desorb atoms or molecules by heating the substrate locally. LITD was carried out in the LEEM using a pulsed Nd:YAG laser ($\lambda = 1064$ nm) with 10 ns pulse width.

Real-time observations of the temporal evolution of non-equilibrium profiles in CO/Pt(111) and Pb/Si(111) towards equilibrium uniform coverage distributions are shown in figure 10. These observations reveal qualitatively that the quasi-Gaussian coverage profile that is produced by LITD in CO/Pt(111) broadens as CO coverage gradually approaches equilibrium uniform distribution (figures 10(a)–(d)). This is the characteristic behavior of mass transport that is governed by the diffusion equation. In the case of Pb/Si(111), however, LEEM observations reveal several surprising features. First, the initial coverage step profile that is produced by LITD is observed to propagate from the edge of the desorption region at approximately constant velocity and with largely unperturbed step profile shape (figures 10(e)–(h)). This is in stark contrast to the characteristic profile broadening that is predicted by the diffusion equation. It has been shown instead to be a signature of convection-like surface mass transport mechanism [141].

The first approach to extracting quantitative information about diffusion from the experimental data is to model profile evolution by numerical solution of the diffusion equation [140]. The general idea of this approach is to predict the correct, i.e. experimentally observed, evolution from a known initial condition and subject to known boundary conditions. This is achieved by appropriate selection of control parameters, the diffusion coefficient here, in the governing diffusion equation. The success of this approach depends crucially on the validity of the governing equation that is used. It also requires that the functional forms of the control parameters are anticipated correctly. The second approach to extracting information about diffusion from the experimental data employs an inverse solution method [140]. Inverse methods have been used in the past to determine thermal conductivity in heat conduction problems. Since the governing equations for heat conduction and mass diffusion are the same, the inverse method is readily adapted to the present problem. Unlike the predictive modeling approach described above, the diffusion coefficient is determined directly at every point in space and time from the data by the inverse method. Schematically, this is done by using the experimentally measured coverage in the neighborhood of a spatial position at one point in time to determine the local coverage gradients, and the measured coverage at that position at consecutive times

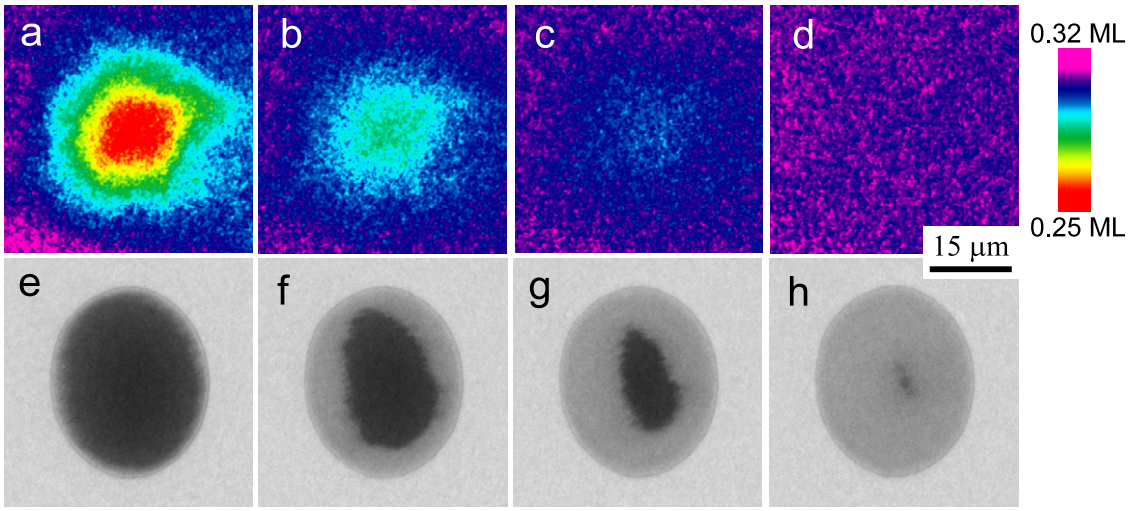


**Figure 10.** LEEM images of non-equilibrium coverage profile evolution at 300 K in (a)–(d) CO/Pt(111) as coverage profiles and (e)–(h) Pb/Si(111) as intensity profiles. The times after (a) are (b) 27.5 s, (c) 55 s and (d)110 s. The times after (e) are (f) 0.6 s, (g) 1.2 s and (h) 2.0 s. Reproduced with permission from [140] and [141]. Copyright 2008 by the American Physical Society.

to determine its time rate of change. This information is used to invert the diffusion equation and solve for the diffusion coefficient locally in space and time. The conservation of mass flowing between neighboring spatial positions in consecutive time steps imposes a constraint that produces a set of coupled equations, which are treated by the finite difference method. From this, information about coverage and position-dependent diffusion can be extracted free of any assumptions. Thus, the value of the inverse solution method, in general, is that it provides information that can serve as a guide for the functional forms of control parameters and governing equation that are used in the traditional predictive modeling approach.

## 5. Complementary diffraction

The diffraction capability of LEEM can be used in several ways that complement imaging and to gain access to information on various length scales that extend below the image spatial resolution. This begins with basic information about the unit cell dimension, symmetry and orientation that is conventionally revealed by the diffraction pattern. In a LEEM instrument, the utility of this elementary characterization can be enhanced by performing measurements at very small length scales using a method called microspot LEED (figure 11) [37, 158–161]. Microspot LEED is carried out by restricting either the area on the surface that is illuminated by the incident beam or the size of the reflected beam that is used to form the diffraction pattern. These restrictions are made by introducing a small aperture in the incident beam or reflected beam on the illumination or imaging side of the sector field, respectively (figure 1). As a rough estimate, a selected area as small as 250 nm should be achievable using a 5 $\mu$m aperture with a 20× demagnification of the objective lens. This capability has been used to reveal domain morphology at short length scales that are usually averaged over in conventional apparatus. It may also prove to be useful for studying individual surface-supported nanostructures in the future.

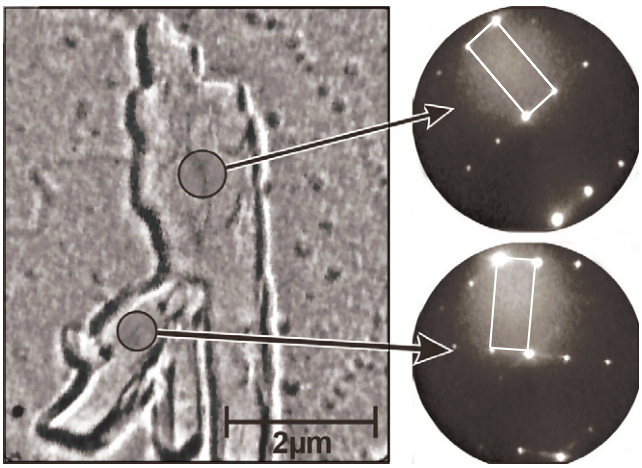


**Figure 11.** Microspot LEED measurements performed in LEEM reveal domain morphology in pentacene on the Au-covered Si(111) surface. Reproduced with permission from [158]. Copyright 2005 by the American Physical Society.

In contrast to the motion of diffraction spots that is observed in a conventional LEED apparatus when the incident energy is changed, diffraction spots are stationary in the diffraction pattern that is visualized by LEEM. This behavior is a consequence of the compensating action of the accelerating field in the objective lens. However, when facets that are inclined from the surface plane are present, characteristic facet diffraction spot motion can still be observed in response to changes of the incident energy. Procedures for the analysis of facet diffraction spot motion in LEEM that account for the objective lens action have been developed, which allow for the determination of the orientation and crystallography of inclined facets [162, 163].

Furthermore, facet diffraction spot analysis in LEEM takes on greater meaning when combined with its microspot

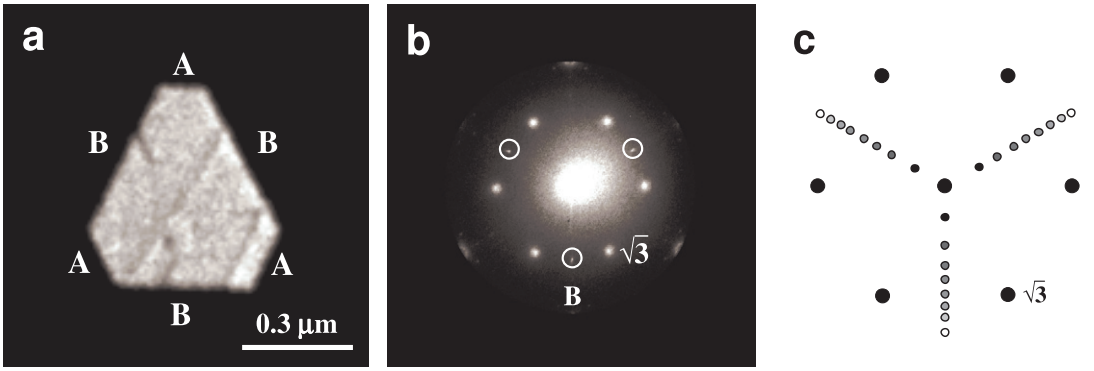


**Figure 12.** (a) LEEM image of a three-dimensional Ag(111) crystal on the Si(111)-Ag $\sqrt{3} \times \sqrt{3}$R30° surface with side facets labeled A and B. (b) LEED pattern of the Ag(111) crystal on Si(111) at 12.4 eV. Diffraction spots from facets B (circled) and from the $\sqrt{3} \times \sqrt{3}$R30° substrate are indicated. (c) A schematic drawing of the LEED pattern at several energies. The small shaded circles indicate the positions of the facet diffraction spots from side facets B at different energies ranging from 7 eV (black) to 14 eV (white). Reproduced with permission from [163]. Copyright 2002 by the American Vacuum Society.

LEED capabilities. This combination can be used to measure facet angles locally at a known position or feature that is observed directly in the LEEM image (figure 12). Facet diffraction can also be harnessed to produce contrast between facets and their surroundings. This novel contrast mechanism was exploited to observe the evolution of Ge/Si three-dimensional islands from pyramid to dome morphology in real-time during growth [124].

Information about features on even shorter length scales is accessible by application of other established methods. In LEED spot profile analysis (SPA), the shapes and widths of diffraction spots are evaluated to obtain information about domain or island size distributions or island height distributions, for example [164]. These measurements are sensitive to features that are shorter than the coherence length of the electron beam, subject to sufficiently high dynamic range of the measured intensity. Although the coherence length, which is typically on the order of a few hundred ångströms, and the dynamic range of the LEED measurement in LEEM are inferior to dedicated SPA-LEED apparatus, spot profile analysis is still a viable means for probing short length scales in LEEM. Examples of an instrumentally-limited LEED spot profile in LEEM and spot profile broadening caused by the proliferation of surface steps during the formation of the W(110)-Ag c(2 × 2) surface alloy are shown in figure 13 [110].

Analysis of LEED intensity versus energy, $I(V)$, curves by dynamical multiple scattering calculations is a traditional method for surface structure determination [17] that can also be pursued in LEEM to some advantage [37, 48, 150, 156, 157, 161, 165–170]. LEED $I(V)$ curve measurements in the LEEM brings several benefits. One advantage is that the specular reflected (00) beam is not obstructed by the sample holder in LEEM as it is in a conventional LEED apparatus. The specular beam intensity has been found to be particularly sensitive to structural details. This advantage of the LEEM-based approach for $I(V)$ structural analysis is partially offset by inherent limitations. In particular, the range of parallel momentum transfer, $\Delta k_{\parallel}$, that is accessible for measurement in the diffraction mode of operation is limited. For low index [(100), (110), (111)] metal surfaces, the range of accessible $\Delta k_{\parallel}$ seldom extends much further away from the (00) spot than the (10), (11) and equivalent diffraction spots. Another limitation of LEEM for LEED $I(V)$ curve measurement is that imaging and diffraction requires normal or near-normal incidence. These two constraints limit the size of the dataset that can be obtained.

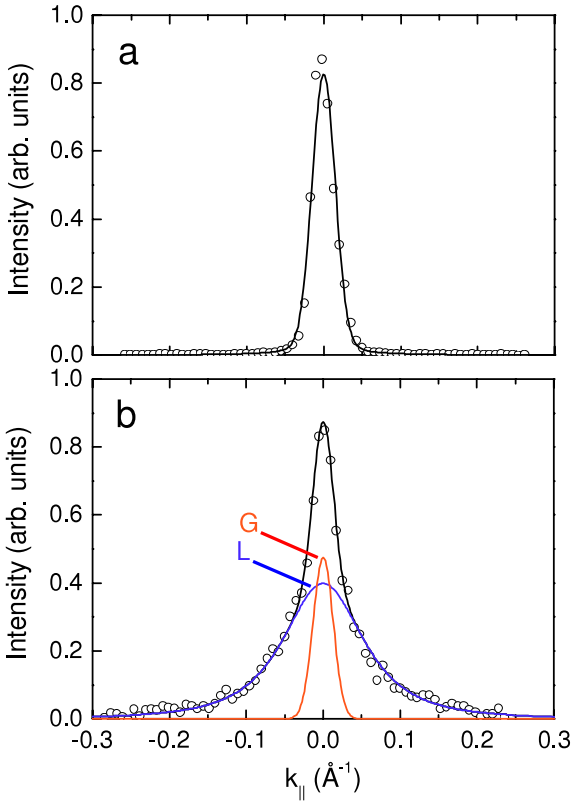


**Figure 13.** The spot profile of the (0, 0) beam at an incident electron energy of 25.0 eV is shown for (a) the clean W(100) surface at 300 K and (b) the W(100)-Ag c(2 × 2) alloy surface at 1095 K. In (a), an instrumentally limited Gaussian lineshape is indicated by the solid curve. In (b) the lineshape (black curve) is composed of a narrow instrumental Gaussian component (G, red curve) and a broad Lorentzian to the 3/2 power component (L, blue curve). Reproduced with permission from [110]. Copyright 2007 by Elsevier.

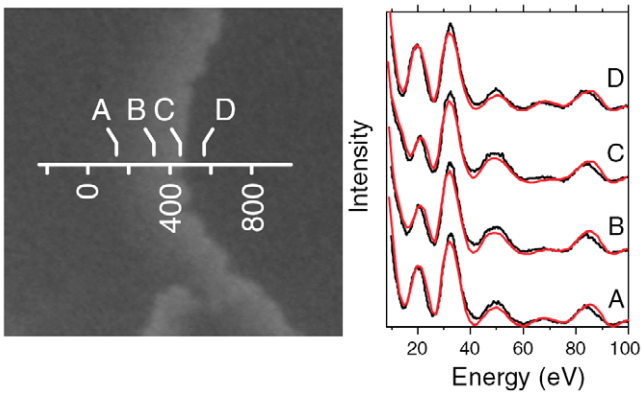


**Figure 14.** A LEEM image recorded at 13.5 eV after the deposition of 0.45 ML of Pd at 200 °C. Distances along the line scan are given in nanometers. At the start of Pd deposition, the step was located at $x = 0$. Measured (computed) $IV$ curves at A, B, C and D are shown in black (red). Reproduced with permission from [150]. Copyright 2006 by the American Physical Society.

Nevertheless, a comparison of $I(V)$ structural analysis using datasets obtained using LEEM and conventional apparatus indicates that the limitations of the LEEM approach do not pose a serious problem [161].

The electron beam is also well shielded from stray fields in LEEM. Thus, $I(V)$ curve measurement can be performed reliably below the conventional minimum, ∼50 eV, without the disturbing effects of beam deflection due to stray fields. This is an interesting realm because the incident wave vector changes more rapidly with energy in this range than at higher energy. Thus, the information content of LEED intensities in the very low energy range is high. Elastic electron scattering is also very sensitive to adsorbates in the very low energy range [140, 171]. However, extraction of structural information from experimental data is not trivial because of several thorny issues relating to electron scattering at very low incident energy that must be treated in the theoretical analysis. These include the energy dependence of inner potential and inelastic scattering and the shape of the surface barrier potential [48, 150, 156, 157, 165–170]. Since the electron penetration depth increases significantly at low energy, a problem with convergence of LEED calculations is another major concern. These issues represent an ongoing area of research that requires greater attention.

LEEM also offers the distinct advantage for $I(V)$ analysis of its complementary imaging capability. This can be used to assess the micron-scale uniformity of structures under investigation. Combined with microspot LEED capability, regions containing defects or other inhomogeneities can be avoided and $I(V)$ measurement can be limited to uniform regions. It also allows for measurements in systems where several structures coexist. This can facilitate the comparison of experimental data to model calculations for ideal uniform structures. Selected-area $I(V)$ curve measurements in diffraction mode of the instrument can also be complemented by spatially resolved $I(V)$ measurements in the imaging mode. Although the $I(V)$ curve dataset that is obtained in the imaging mode is severely limited to the (00) beam at normal incidence, it has been shown that this approach can be used to obtain structural information for various lateral length scales approaching the spatial resolution of the instrument (figures 6 and 14) [48, 150, 156, 157, 169]. In the highest resolution measurements to date, this method was used to determine how the three-dimensional composition profile of an alloy film evolves during growth at the several nanometer length scale [150, 169]. This appears to be a very promising avenue for pushing LEED structure analysis to the nanoscale.

## 6. Conclusions

The sensitivities, spatial and temporal resolutions of LEEM and SPLEEM have been exploited for many years to expand our understanding of surfaces, thin films and surface-supported nanostructures in a variety of materials systems. Progress has been made and will continue to be made by understanding the sensitivities provided by various contrast mechanisms and by applying this understanding in image interpretation. Although phase contrast seems to be in hand, diffraction or reflectivity contrast is just beginning to yield quantitative information at short length scales that are accessible in LEEM down to image resolution. Potentials of LEEM and SPLEEM lie in creative use of existing imaging and complementary diffraction capabilities as well as new capabilities that come with advances in methodology and instrumentation. With the development of aberration-corrected instruments, we are now on the brink of the most dramatic improvement of image spatial resolution in many years. On the other hand, temporal resolution, which is an attractive property of LEEM, has been stagnant or even taken a step backward with the advent of image recording from microchannel plate/phosphor screen detectors using high resolution, high dynamic range ccd cameras. In the case of SPLEEM, progress in this area may come as the result of recent and ongoing developments of brighter spin polarized electron sources. Otherwise, fundamental changes in signal detection may offer some hope for a breakthrough in the future.

## References

[1] Bauer E 1962 Electron microscopy *Fifth Int. Congr. for Electron Microscopy* vol 1, ed S S Breese Jr (New York: Academic) p D-11
[2] Bauer E 1994 *Rep. Prog. Phys.* **57** 895
[3] Bauer E 1998 *Surf. Rev. Lett.* **5** 1275
[4] Tromp R M 2000 *IBM J. Res. Dev.* **44** 503
[5] Phaneuf R J and Schmid A K 2003 *Phys. Today* **56** (3) 50
[6] Bauer E 2007 *Science of Microscopy* ed P W Hawkes and J C H Spence (New York: Springer) pp 606–56
[7] Telieps W and Bauer E 1985 *Ultramicroscopy* **17** 57
[8] Tromp R M and Reuter M C 1991 *Ultramicroscopy* **36** 99
[9] Veneklasen L H 1991 *Ultramicroscopy* **36** 76
[10] Veneklasen L H 1992 *Rev. Sci. Instrum.* **63** 5513
[11] Grzelakowski K, Duden T, Bauer E, Poppa H and Chiang S 1994 *IEEE Trans. Magn.* **30** 4500
[12] Grzelakowski K and Bauer E 1996 *Rev. Sci. Instrum.* **67** 742
[13] Tromp R M, Mankos M, Reuter M C, Ellis A W and Copel M 1998 *Surf. Rev. Lett.* **5** 1189
[14] Adamec P, Bauer E and Lencova B 1998 *Rev. Sci. Instrum.* **69** 3583
[15] Mankos M, Adler D, Veneklasen L and Munro E 2007 *Surf. Sci.* **601** 4733

[16] Chmelik J, Veneklasen L and Marx G 1989 *Optik* **83** 155
[17] van Hove M A, Weinberg W A and Chan C M 1986 *Low Energy Electron Diffraction* (Berlin: Springer)
[18] Bauer E 1985 *Ultramicroscopy* **17** 51
[19] Rempfer G F, Desloge D M, Skoczylas W P and Griffith O H 1997 *Microsc. Microanal.* **3** 14
[20] Wichtendahl R *et al* 1998 *Surf. Rev. Lett.* **5** 1249
[21] Schmidt Th *et al* 2002 *Surf. Rev. Lett.* **9** 223
[22] Tromp R M 2006 unpublished
[23] Schmidt Th 2006 private communication
[24] Pang A B, Müller Th, Altman M S and Bauer E 2009 *J. Phys.: Condens. Matter* **21** 314006
[25] Telieps W, Mundschau M and Bauer E 1987 *Optik* **77** 93
[26] Telieps W, Mundschau M and Bauer E 1990 *Surf. Sci.* **225** 87
[27] Telieps W 1987 *Appl. Phys.* A **44** 55
[28] Mundschau M, Bauer E, Telieps W and Święch W 1989 *Surf. Sci.* **223** 413
[29] Bartelt N C, Tromp R M and Williams E D 1994 *Phys. Rev. Lett.* **73** 1656
[30] Thies W, Bartelt N C and Tromp R M 1995 *Phys. Rev. Lett.* **75** 3328
[31] Jones D E, Pelz J P, Hong Y, Bauer E and Tsong I S T 1996 *Phys. Rev. Lett.* **77** 330
[32] Hannon J B, Bartelt N C, Swartzentruber B S, Hamilton J C and Kellogg G L 1997 *Phys. Rev. Lett.* **79** 4226
[33] Tanaka S, Bartelt N C, Umbach C C, Tromp R M and Blakely J M 1997 *Phys. Rev. Lett.* **78** 3342
[34] Hannon J B, Shenoy V B and Schwarz K W 2006 *Science* **313** 1266
[35] Maxson J B, Perkins N, Savage D E, Woll A R, Zhang L, Kuech T F and Lagally M G 2000 *Surf. Sci.* **464** 217
[36] Hibino H and Watanabe Y 2005 *Japan. J. Appl. Phys.* **44** 358
[37] de la Figuera J, Puerta J M, Cerda J I, El Gabaly F and McCarty K F 2006 *Surf. Sci.* **600** L105
[38] Chung W F and Altman M S 1998 *Ultramicroscopy* **74** 237
[39] Altman M S, Chung W F and Liu C H 1998 *Surf. Rev. Lett.* **5** 1129
[40] Thomas R 1970 *J. Appl. Phys.* **41** 5330
[41] Jonker B T, Bartelt N C and Park R L 1983 *Surf. Sci.* **127** 183
[42] Jaklevic R C 1984 *Phys. Rev.* B **30** 5494
[43] Kerkmann D, Pescia D, Krewer J W and Vescovo E 1991 *Z. Phys.* B **85** 311
[44] Mundschau M, Bauer E and Święch W 1989 *J. Appl. Phys.* **65** 581
[45] Scheunemann T, Feder R, Henk J, Bauer E, Duden T, Pinkvos H, Poppa H and Wurm K 1997 *Solid State Commun.* **104** 787
[46] Altman M S, Chung W F, He Z Q, Poon H C and Tong S Y 2001 *Appl. Surf. Sci.* **169/170** 82
[47] Zdyb R and Bauer E 2002 *Phys. Rev. Lett.* **88** 166403
[48] Chung W F, Feng Y J, Poon H C, Chan C T, Tong S Y and Altman M S 2003 *Phys. Rev. Lett.* **90** 216105
[49] Man K L, Qiu Z Q and Altman M S 2004 *Phys. Rev. Lett.* **93** 236104
[50] Aballe L, Barinov A, Locatelli A, Heun S and Kiskinova M 2004 *Phys. Rev. Lett.* **93** 196103
[51] Ling W L, Giessel T, Thürmer K, Hwang R Q, Bartelt N C and McCarty K F 2004 *Surf. Sci.* **570** L297
[52] Altman M S 2005 *J. Phys.: Condens. Matter* **17** S1305
[53] Wu Y Z, Schmid A K, Altman M S, Jin X F and Qiu Z Q 2005 *Phys. Rev. Lett.* **94** 027201
[54] Graf J, Jozwiak C, Schmid A K, Hussain Z and Lanzara A 2005 *Phys. Rev.* B **71** 144429
[55] Ling W L, Bartelt N C, McCarty K F and Carter C B 2005 *Phys. Rev. Lett.* **95** 166105
[56] Man I K H and Altman M S 2005 *Surf. Interface Anal.* **37** 235
[57] Wu Y Z, Schmid A K and Qiu Z Q 2006 *Phys. Rev. Lett.* **97** 217205
[58] Ling W L, Hamilton J C, Thürmer K, Thayer G E, de la Figuera J, Hwang R Q, Carter C B, Bartelt N C and McCarty K F 2006 *Surf. Sci.* **600** 1735
[59] McCarty K F 2006 *Nano Lett.* **6** 858
[60] Aballe L Barinov A, Locatelli A, Mentes T O and Kiskinova M 2007 *Phys. Rev.* B **75** 115411
[61] Hibino H, Kageshima H, Maeda F, Nagase M, Kobayashi Y and Yamaguchi H 2008 *Phys. Rev.* B **77** 075413
[62] Ohta T, El Gabaly F, Bostwick A, McChesney J L, Emtsev K V, Schmid A K, Seyller T, Horn K and Rotenberg E 2008 *New J. Phys.* **10** 023034
[63] Knox K R, Wang S, Morgante A, Cvetko D, Locatelli A, Mentes T O, Niño M A, Kim P and Osgood R M Jr 2008 *Phys. Rev.* B **78** 201408R
[64] Emtsev K V *et al* 2009 *Nat. Mater.* **8** 203
[65] Smith N V, Brookes N B, Chang Y and Johnson P D 1994 *Phys. Rev.* B **49** 332
[66] Altman M S, Pinkvos H, Hurst J, Poppa H, Marx G and Bauer E 1991 *Mater. Res. Soc. Symp. Proc.* **232** 125–32
[67] Poppa H, Bauer E and Pinkvos H 1995 *MRS Bull.* **20** 38
[68] Bauer E, Duden T and Zdyb R 2002 *J. Phys. D: Appl. Phys.* **35** 2327
[69] Bauer E 2005 *Magnetic Microscopy of Nanostructures* ed H Hopster and H P Oepen (Berlin: Springer) pp 111–36
[70] Bauer E 2007 *The Handbook of Magnetism and Advanced Magnetic Materials* vol 3, ed H Kronmueller and S Parkin (Chichester: Wiley) pp 1470–82
[71] Pierce D T, Cellota R J, Wang G C, Unertl W N, Galejs A, Kuyatt C E and Mielczarek S R 1980 *Rev. Sci. Instrum.* **51** 478
[72] Murayama T, Garwin E L, Prepost R, Zapalac G H, Smith J S and Walker J D 1991 *Phys. Rev. Lett.* **66** 2376
[73] Nakanishi T, Aoyagi H, Horinaka H, Kamiya Y, Kato T, Nakamura S, Saka T and Tsubata M 1991 *Phys. Lett.* A **158** 345
[74] Nakanishi T *et al* 2000 *Nucl. Instrum. Methods Phys. Res.* A **455** 109
[75] Yamamoto N *et al* 2008 *J. Appl. Phys.* **103** 064905
[76] Jin X *et al* 2008 *Appl. Phys. Express* **1** 045002
[77] Jin X *et al* 2008 *J. Cryst. Growth* **310** 5039
[78] Duden T and Bauer E 1995 *Rev. Sci. Instrum.* **66** 2861
[79] Man K L, Zdyb R, Huang S F, Leung T C, Chan C T, Bauer E and Altman M S 2003 *Phys. Rev.* B **67** 184402
[80] Duden T and Bauer E 1996 *Phys. Rev. Lett.* **77** 2308
[81] Duden T and Bauer E 1997 *Mater. Res. Soc. Symp. Proc.* **475** 283–8
[82] Duden T and Bauer E 1999 *Phys. Rev.* B **59** 468
[83] Duden T, Zdyb R, Altman M S and Bauer E 2001 *Surf. Sci.* **480** 145
[84] Man K L, Altman M S and Poppa H 2001 *Surf. Sci.* **480** 163
[85] Man K L, Ling W L, Paik S Y, Poppa H, Altman M S and Qiu Z Q 2001 *Phys. Rev.* B **65** 024409
[86] Zdyb R and Bauer E 2003 *Phys. Rev.* B **67** 134420
[87] Ramchal R, Schmid A K, Farle M and Poppa H 2003 *Phys. Rev.* B **68** 054418
[88] Ding H F, Schmid A K, Li D, Guslienko K Y and Bader S D 2005 *Phys. Rev. Lett.* **94** 157202
[89] Zdyb R, Pavlovska A, Jałochowski M and Bauer E 2006 *Surf. Sci.* **600** 1586
[90] Rougemaille N and Schmid A K 2006 *J. Appl. Phys.* **99** 08S502
[91] Rougemaille N, Portalupi M, Brambilla A, Biagioni P, Lanzara A, Finazzi M, Schmid A K and Duo L 2007 *Phys. Rev.* B **76** 214425
[92] Duden T and Bauer E 1999 *J. Magn. Mater.* **191** 301
[93] Duden T and Bauer E 1999 *Phys. Rev.* B **59** 474
[94] Ramchal R, Schmid A K, Farle M and Poppa H 2004 *Phys. Rev.* B **69** 214401
[95] El Gabaly F, Gallego S, Muñoz C, Szunyogh L, Weinberger P, Klein C, Schmid A K, McCarty K F and de la Figuera J 2006 *Phys. Rev. Lett.* **96** 147202
[96] Klein C, Ramchal R, Farle M and Schmid A K 2006 *Surf. Interface Anal.* **38** 1550

[97] Klein C, Ramchal R, Schmid A K and Farle M 2007 *Phys. Rev.* B **75** 193405
[98] El Gabaly F, McCarty K F, Schmid A K, de la Figuera J, Muñoz M C, Szunyogh L, Weinberger P and Gallego S 2008 *New J. Phys.* **10** 073024
[99] Zdyb R and Bauer E 2008 *Phys. Rev. Lett.* **100** 155704
[100] Poppa H, Tober E D and Schmid A K 2002 *J. Appl. Phys.* **91** 6932
[101] Koshikawa T 2009 private communication
[102] Telieps W and Bauer E 1985 *Surf. Sci.* **162** 163
[103] Tromp R M, Theis W and Bartelt N C 1996 *Phys. Rev. Lett.* **77** 2522
[104] Hannon J B and Tromp R M 2000 *Annu. Rev. Mater. Res.* **33** 263
[105] Hannon J B, Hibino H, Bartelt N C, Swartzentruber B S, Ogino T and Kellogg G L 2000 *Nature* **405** 552
[106] Maxson J B, Savage D E, Liu F, Tromp R M, Reuter M C and Lagally M G 2000 *Phys. Rev. Lett.* **85** 2152
[107] van Vroonhoven E, Zandvliet H J W and Poelsema B 2003 *Phys. Rev. Lett.* **91** 116102
[108] Pavlovska A and Bauer E 2005 *Surf. Interface Anal.* **37** 110
[109] Sato Y, Chiang S and Bartelt N C 2007 *Phys. Rev. Lett.* **99** 096103
[110] Man K L, Feng Y J, Chan C T and Altman M S 2007 *Surf. Sci.* **601** L95
[111] Plass R, Last J A, Bartelt N C and Kellogg G L 2001 *Nature* **412** 875
[112] Nielsen J F, Pelz J P, Hibino H, Hu C W, Tsong I S T and Kouvetakis J 2001 *Appl. Phys. Lett.* **79** 3857
[113] van Gastel R, Plass R, Bartelt N C and Kellogg G L 2003 *Phys. Rev. Lett.* **91** 055503
[114] van Gastel R, Bartelt N C, Feibelman P J, Léonard F and Kellogg G L 2004 *Phys. Rev.* B **70** 245413
[115] Meyer zu Heringdorf F J, Schmidt Th, Heun S, Hild R, Zahl P, Ressel B, Bauer E and Horn-von Hoegen M 2001 *Phys. Rev. Lett.* **86** 5088
[116] Hannon J B, Tersoff J and Tromp R M 2002 *Science* **295** 299
[117] Sutter P, Bennett P A, Flege J I and Sutter E 2007 *Phys. Rev. Lett.* **99** 125504
[118] Mentes T O, Locatelli A, Aballe L and Bauer E 2007 *Phys. Rev. Lett.* **101** 085701
[119] Schmidt Th, Flege J I, Gangopadhyay S, Clausen T, Locatelli A, Heun S and Falta J 2007 *Phys. Rev. Lett.* **98** 066104
[120] de la Figuera J, Léonard F, Bartelt N C, Stumpf R and McCarty K F 2008 *Phys. Rev. Lett.* **100** 186102
[121] Schmidt Th and Bauer E 2000 *Phys. Rev.* B **62** 15815
[122] Yasue T, Koshikawa T, Jałochowski M and Bauer E 2000 *Surf. Rev. Lett.* **7** 595
[123] Hannon J B, Hibino H, Bartelt N C, Swartzentruber B S, Ogino T and Kellogg G L 2000 *Nature* **405** 552
[124] Ross F M, Tromp R M and Reuter M C 1999 *Science* **286** 1931
[125] McCarty K F, Nobel J A and Bartelt N C 2001 *Nature* **412** 622
[126] Gerlach R, Maroutian T, Douillard L, Martinotti D and Ernst H J 2001 *Surf. Sci.* **480** 97
[127] Hibino H, Hu C W, Ogino T and Tsong I S T 2001 *Phys. Rev.* B **63** 245402
[128] Chung W F and Altman M S 2002 *Phys. Rev.* B **66** 075338
[129] Poelsema B, Hannon J B, Bartelt N C and Kellogg G L 2004 *Appl. Phys. Lett.* **84** 2551
[130] Kodambaka S, Khare S V, Święch W, Ohmori K, Petrov I and Greene J E 2004 *Nature* **429** 49
[131] Hibino H, Homma Y, Hu C W, Uwaha M, Ogino T and Tsong I S T 2004 *Appl. Surf. Sci.* **237** 51
[132] Kellogg G L and Bartelt N C 2005 *Surf. Sci.* **577** 151
[133] Tang S J, Kodambaka S, Swiech W, Petrov I, Flynn C P and Chiang T C 2006 *Phys. Rev. Lett.* **96** 126106
[134] de la Figuera J, Bartelt N C and McCarty K F 2006 *Surf. Sci.* **600** 4062
[135] Man K L, Guo Q and Altman M S 2006 *Surf. Sci.* **600** 1060
[136] Hibino H, Uematsu M and Watanabe Y 2006 *J. Appl. Phys.* **100** 113519
[137] Anderson M L, Bartelt N C, Feibelman P J, Swartzentruber B S and Kellogg G L 2007 *Phys. Rev. Lett.* **98** 096106
[138] Man K L, Pang A B and Altman M S 2007 *Surf. Sci.* **601** 4669
[139] Loginova E, Bartelt N C, Feibelman P J and McCarty K F 2008 *New J. Phys.* **10** 093026
[140] Yim C M, Man K L, Xiao X and Altman M S 2008 *Phys. Rev.* B **78** 155439
[141] Man K L, Tringides M C, Loy M M T and Altman M S 2008 *Phys. Rev. Lett.* **101** 226102
[142] Hibino H, Kageshima H and Uwaha M 2008 *Surf. Sci.* **602** 2421
[143] Ondrejcek M, Swiech W, Petrov I, Rajappan M and Flynn C P 2009 *Microsc. Res. Tech.* **72** 197
[144] Tromp R M and Hannon J B 2009 *Phys. Rev. Lett.* **102** 106014
[145] Ondrejcek M, Święch W, Rajappan M and Flynn C P 2005 *Phys. Rev.* B **72** 085422
[146] Pang A B, Man K L, Altman M S, Stasevich T, Szalma F and Einstein T L 2008 *Phys. Rev.* B **77** 115424
[147] Wu D, Lau W K, He Z Q, Feng Y J, Altman M S and Chan C T 2000 *Phys. Rev.* B **62** 8366
[148] Hannon J B, Copel M, Stumpf R, Reuter M C and Tromp R M 2004 *Phys. Rev. Lett.* **92** 216104
[149] Hibino H and Watanabe Y 2005 *Surf. Sci.* **588** L233
[150] Hannon J B, Sun J, Pohl K and Kellogg G L 2006 *Phys. Rev. Lett.* **96** 246103
[151] Man K L, Feng Y J and Altman M S 2006 *Phys. Rev.* B **74** 085420
[152] Altman M S and Bauer E 1996 *Surf. Sci.* **347** 265
[153] Hannon J B, Bartelt M C, Bartelt N C and Kellogg G L 1998 *Phys. Rev. Lett.* **81** 4676
[154] Schmidt Th, Schaak A, Günther S, Ressel B, Bauer E and Imbihl R 2000 *Chem. Phys. Lett.* **318** 549
[155] Locatelli A, Aballe L, Mentes T O, Guo F Z and Kiskinova M 2007 *Surf. Sci.* **601** 4663
[156] Flege J I and Sutter P 2008 *Phys. Rev.* B **78** 153402
[157] Flege J I, Hrbek J and Sutter P 2008 *Phys. Rev.* B **78** 165407
[158] Thayer G E, Sadowski J T, Meyer zu Heringdorf F, Sakurai T and Tromp R M 2005 *Phys. Rev. Lett.* **95** 256106
[159] Locatelli A, Pabisiak T, Pavlovska A, Mentes T O, Aballe L, Kiejna A and Bauer E 2007 *J. Phys.: Condens. Matter* **19** 082202
[160] Sadowski J T, Sazaki G, Nishikata S, Al-Mahboob A, Fujikawa Y, Nakajima K, Tromp R M and Sakurai T 2007 *Phys. Rev. Lett.* **98** 046104
[161] Reichelt R, Günther S, Wintterlin J, Moritz W, Aballe L and Mentes T O 2007 *J. Chem. Phys.* **127** 134706
[162] Yasue T, Koshikawa T, Jałochowski M and Bauer E 2001 *Surf. Sci.* **493** 381
[163] Tang W X, Man K L, Huang H, Woo C H and Altman M S 2002 *J. Vac. Sci. Technol.* B **20** 2492
[164] Horn-von Hoegen M 1999 *Z. Kristallogr.* **214** 591
[165] Bartoš I, Jaroš P, Barbieri A, van Hove M A, Chung W F, Cai Q and Altman M S 1995 *Surf. Rev. Lett.* **2** 477
[166] Bartoš I, van Hove M A and Altman M S 1996 *Surf. Sci.* **352–354** 660
[167] Bartoš I, van Hove M A, Chung W F, He Z and Altman M S 1998 *Surf. Sci.* **402–404** 697
[168] Poon H C, Tong S Y, Chung W F and Altman M S 1998 *Surf. Rev. Lett.* **5** 1143
[169] Sun J, Hannon J B, Kellogg G L and Pohl K 2007 *Phys. Rev.* B **76** 205414
[170] Sutter P W, Flege J I and Sutter E A 2008 *Nat. Mater.* **7** 406
[171] Pfnür H, Lindroos M and Menzel D 1991 *Surf. Sci.* **248** 1